Laser-Induced Electron Tunneling and Diffraction

Meckel, M.; Comtois, D.; Zeidler, D.; Staudte, A.; Pavičić, D.; Bandulet, H. C.; Pépin, H.; Kieffer, J. C.; Dörner, R.; Villeneuve, D. M.; Corkum, P. B.

Publisher's version / Version de l'éditeur:
https://doi.org/10.1126/science.1157980
Science, 320, pp. 1478-1481, 2008-05-01

5. K. S. Egiyan *et al.*, *Phys. Rev. Lett.* **96**, 082501 (2006).
6. R. A. Niyazov *et al.*, *Phys. Rev. Lett.* **92**, 052303 (2004).
7. F. Benmokhtar *et al.*, *Phys. Rev. Lett.* **94**, 082305 (2005).
8. J. L. S. Aclander *et al.*, *Phys. Lett. B* **453**, 211 (1999).
9. A. Tang *et al.*, *Phys. Rev. Lett.* **90**, 042301 (2003).
10. A. Malki *et al.*, *Phys. Rev. C Nucl. Phys.* **65**, 015207 (2002).
11. E. Piasetzky, M. Sargsian, L. Frankfurt, M. Strikman, J. W. Watson, *Phys. Rev. Lett.* **97**, 162504 (2006).
12. R. Shneor *et al.*, *Phys. Rev. Lett.* **99**, 072501 (2007).
13. L. L. Frankfurt, M. I. Strikman, *Phys. Rep.* **76**, 215 (1981).
14. L. L. Frankfurt, M. I. Strikman, D. B. Day, M. Sargsian, *Phys. Rev. C Nucl. Phys.* **48**, 2451 (1993).
15. J. Alcorn *et al.*, *Nucl. Instrum. Methods* **A522**, 294 (2004).
16. Materials and methods are available as supporting material on *Science* Online.
17. I. Mardor, Y. Mardor, E. Piasetzky, J. Alster, M. M. Sargsian, *Phys. Rev. C Nucl. Phys.* **46**, 761 (1992).
18. R. Schiavilla, R. B. Wiringa, S. C. Pieper, J. Carlson, *Phys. Rev. Lett.* **98**, 132501 (2007).
19. M. M. Sargsian, T. V. Abrahamyan, M. I. Strikman, L. L. Frankfurt, *Phys. Rev. C Nucl. Phys.* **71**, 044615 (2005).
20. J. M. Lattimer, M. Prakash, *Science* **304**, 536 (2004).
21. G. Baym, *Nucl. Phys. A.* **590**, 233 (1995).
22. G. Baym, *Nucl. Phys. A.* **702**, 3 (2002).
23. T. Frick, H. Muther, A. Rios, A. Polls, A. Ramos, *Phys. Rev. C Nucl. Phys.* **71**, 014313 (2005).
24. This work was supported by the Israel Science Foundation, the U.S.-Israeli Binational Scientific Foundation, the UK Engineering and Physical Sciences Research Council and Science and Technology Facilities Council, NSF, and the U.S. Department of Energy (DOE) (grants DE-AC02-06CH11357 and DE-FG02-94ER40818 and U.S. DOE contract no. DE-AC05-84150, modification no. M175, under which the Southeastern Universities Research Association, Inc. operates the Thomas Jefferson National Accelerator Facility). The raw data from this experiment are archived in Jefferson Lab's mass storage silo.

Supporting Online Material

www.sciencemag.org/cgi/content/full/320/5882/1476/DC1
Materials and Methods
Figs. S1 and S2
Table S1
References

19 February 2008; accepted 8 May 2008
10.1126/science.1156675

Laser-Induced Electron Tunneling and Diffraction

M. Meckel,[1,2] D. Comtois,[3] D. Zeidler,[1,4] A. Staudte,[1,2] D. Pavičić,[1] H. C. Bandulet,[3] H. Pépin,[3] J. C. Kieffer,[3] R. Dörner,[2] D. M. Villeneuve,[1] P. B. Corkum[1]*

Molecular structure is usually determined by measuring the diffraction pattern the molecule impresses on x-rays or electrons. We used a laser field to extract electrons from the molecule itself, accelerate them, and in some cases force them to recollide with and diffract from the parent ion, all within a fraction of a laser period. Here, we show that the momentum distribution of the extracted electron carries the fingerprint of the highest occupied molecular orbital, whereas the elastically scattered electrons reveal the position of the nuclear components of the molecule. Thus, in one comprehensive technology, the photoelectrons give detailed information about the electronic orbital and the position of the nuclei.

Molecular multiphoton ionization in the tunneling limit (sketched in the upper frame of Fig. 1) is similar to tunneling in a scanning tunneling microscope (STM) (*1*). In both cases, electrons escape from the outer regions of the orbital to the continuum; that is, to the vacuum for multiphoton ionization of gas phase molecules or to the conduction band of the metal tip in a STM. In a STM, the sample is fixed and the tip is moved. Rotating the molecule with respect to the field direction is the analog of moving the tip. The resulting angle-dependent ionization probability (*2*–*5*) provides information for a molecule analogous to the position dependence of the tunneling current in a STM. However, whereas the total tunneling current is one observable, the electron wave packet that emerges into the vacuum from the tunnel retains more information about the orbital.

In contrast to the static field of a STM, the electric field in a laser pulse oscillates and forces a fraction of the tunneled electron wave packet back to the parent ion. There, the wave packet can diffract from the molecule (lower frame in Fig. 1). This phenomenon has been called laser-induced electron diffraction (LIED) (*6*) and relates to recent research on ultrafast electron diffraction, where a femtosecond electron bunch is created at a photocathode and accelerated in an electrostatic field onto a molecular (*7*) or solid state (*8*) target. In our case, the molecule serves as its own photocathode, whereas the laser provides the accelerating field. This situation produces extremely high current densities and attosecond timing (*9*).

We report the observation of molecular tunneling spectroscopy and LIED. We measured electrons produced from aligned O_2 and N_2, resolving their three-dimensional (3D) momentum distribution. Comparing experiment and theory, we show that, in the two dimensions perpendicular to the field direction, the momentum distribution for these direct electrons is determined by the highest occupied molecular orbital (HOMO), observed through the filter of the suppressed binding potential (Fig. 1) through which the electron tunnels. We also demonstrate LIED (*6*) and confirm its origin with a simulation. Selecting the wavelength of the recollision electron modifies the diffraction pattern. Thus, one set of measurements simultaneously identifies the orbital wave function of the molecule and the position of the atoms in the molecule.

Laser-induced tunneling and diffraction exploit different parts of the ionizing electron wave packet. The fraction of the electron wave packet that is created while the field strength increases within an optical half-cycle departs directly and irrevocably from its parent ion. Only tunneling stands between the orbital and the electron detector. The wave packet that is born while the field decreases returns to the ion where it can elastically scatter (diffract), inelastically scatter, or recombine to (interfere with) the orbital from which it was extracted (*10*). These three scattering processes offer different perspectives on the molecule.

Tunneling, the process underlying all, probes the electronic structure of the neutral molecule. The recombination radiation, known as high-harmonic radiation, also measures the orbital structure of the neutral molecule (*11*). However, because high-harmonic generation starts with tunneling and ends with interference, these processes must be disentangled before the techniques can be generalized to complex orbitals. In contrast, elastic and inelastic scattering occur at the molecular ion. Inelastic rescattering is closely related to field-free collision physics (*12*, *13*). It can cause multiple ionization and subsequently lead to Coulomb explosion of small molecules. The molecular structure can then be inferred from the momentum vectors of the correlated ionic fragments. Elastic scattering is also sensitive to the potential structure of the molecular ion. However, here the molecular structure is encoded in the diffracting electron wave packet, making this imaging technique scaleable to more complex molecules.

For electron diffraction to be observable, the de Broglie wavelength of the electron needs to be on the order of the dimensions of the molecule. Small diatomic molecules have a bond length of ≈1 Å [1.9 atomic units (au)]. To obtain this wavelength, an electron would need a kinetic energy of 150 eV, corresponding to a momentum of 3.3 au. Electrons that are accelerated in the laser field and recollide with the parent molecule can easily reach this range of kinetic energies (*10*).

We recorded the momentum of electrons arising from tunneling ionization of aligned O_2 and N_2, employing a Cold Target Recoil Ion Mo-

[1]National Research Council of Canada, 100 Sussex Drive, Ottawa, Ontario, Canada, K1A 0R6. [2]Institut für Kernphysik, Johann Wolfgang Goethe Universität, Max-von-Laue Straße 1, D-60438 Frankfurt, Germany. [3]Institut National de la Recherche Scientifique–Énergie, Matériaux et Télécommunication, 1650 boulevard Lionel-Boulet, Varennes, Québec, Canada, J3X 1S2. [4]Carl Zeiss SMT AG, Rudolf-Eber-Straße 2, 73447 Oberkochen, Germany.

*To whom correspondence should be addressed. E-mail: paul.corkum@nrc.ca

mentum Spectroscopy (COLTRIMS) system (*14*). COLTRIMS allows us to measure the 3D momentum vectors of single electrons and ions in coincidence. This coincidence capability is used to measure both O_2 and N_2 simultaneously under identical conditions by means of a gas mixture. It also allows us to eliminate any contribution to the electron spectra from inelastic scattering resulting in fragmentation or multiple ionization of the molecules. However, with monomolecular targets, we achieve very similar results even without the ion-electron coincidence requirement. Finally, the coincidence measurement permits us to pick up weak fragmentation channels that provide information about the quality of our alignment [see supporting online material (SOM) text B].

Our laser pulse (800 nm) had a total energy of 5 μJ (split and used for both alignment and probing) and a repetition rate of 30 kHz. We align the molecules (*15*) using a slightly stretched (60 fs), moderately intense ($\leq 8 \times 10^{13}$ W/cm^2) laser pulse. The intense (2.5×10^{14} W/cm^2), short (40 fs), ionizing pulse, which is applied after a delay, catches the molecule at any alignment that can be achieved with polarized light. Experimentally, aligning (pump) and ionizing (probe) pulses are perpendicularly polarized (*y* axis and *z* axis in the inset of Fig. 2A, respectively). The pump pulse creates a rotational wave packet (*15*) that results in molecules aligned primarily along the *y* axis at a well-defined time delay (sketch in Fig. 2A). At a different time delay, the alignment distribution will be confined in the *xz* plane (sketch in Fig. 2B). We refer to this complementary case as anti-alignment. A computerized delay stage moved between the respective pump-probe delays every 10 s (details in SOM text A and B).

The electron momentum distributions (Fig. 2) obtained for aligned (A) and anti-aligned (B) O_2 molecules have been correlated with singly charged O_2^+ ions. For display purposes, the distribution is projected onto three planes. Most prominent in the figure is the large dynamic range in the distribution. The color code covers five orders of magnitude. The rapid fall-off of the signal is so prominent that it is hard to discern anything else from the figure. The spectra for N_2 (fig. S1) are qualitatively indistinguishable from those of O_2.

Molecular specific structure arising from tunneling and diffraction is revealed when we employ normalized differences. The anti-aligned projections are subtracted from the aligned projections and then divided by their sum. The normalized differences for O_2 and N_2 are plotted in Fig. 2, C and D. Because the data are not symmetrized, the quadrant-to-quadrant reproducibility is a measure of the quality of the image.

The low lateral-momentum electrons ($p_\perp = \sqrt{p_x^2 + p_y^2} < 0.5$ au, where p is momentum) exhibit clear patterns in the projection perpendicular to the ionizing laser field. The vast majority of these electrons drift directly to the detector without further interaction with the parent ion. They provide information on the ionizing orbital, filtered by the tunnel. These electrons are equally evident in the other two projections. They are spread along the *z* direction between $|p_z| < 1.5$ au, reflecting the fact that ionization can occur over a range of times within a field cycle.

Figure 3 presents an expanded view of the p_x-p_y projections of the electron momenta from N_2 and O_2 and focuses on the central part of the distribution. The very different distributions created by tunneling from O_2 and N_2 reflect the very different structures of the respective ionizing orbitals. In tunneling theory, the tunnel serves as a filter for the perpendicular component $p_\perp$ of the orbital wave function. The tunneled wave packet then can be expressed as (in atomic units) (*16*–*18*)

$$\Psi(p_\perp) \propto \langle p_\perp | \Psi_i \rangle \exp\left(-\frac{\sqrt{I_p}}{\sqrt{2}E} p_\perp^2\right) \quad (1)$$

where the exponential factor is the filter function. It contains the ionization potential I_p and the electric field E of the ionizing laser pulse at the moment of tunneling. The exponential factor depends only weakly on the alignment of the molecule (through a weakly angular-dependent Stark-shift). Therefore, it is approximately cancelled in any ratio of two different alignments. However, the electronic wave function $|\Psi_i\rangle$ is locked to the molecular frame, whereas $p_\perp$ is defined with respect to the laser-field direction. Therefore, the alignment dependence of the projected wave function $\langle p_\perp | \Psi_i \rangle$ is accentuated by taking ratios. We now show that this basic tunneling concept agrees with our experimental measurements.

Using the wave function for the HOMOs of N_2 and O_2, we calculated the lateral electron momentum distributions (both shape and amplitude) that emerge from the molecules for each molecular alignment. The electrons are given initial conditions determined by tunneling and then classically propagated in the field of a pulse identical to the experiment, taking into account the parent ion's Coulomb potential (*19*, *20*). Finally, each molecular alignment contributes to the predicted spectrum, according to its weight in the measured alignment or anti-alignment distribution. There are no free parameters in this model (described more fully in SOM text C). The results are shown in the bottom row of Fig. 3. The simulation reproduces the symmetry seen in the experiment. The model also shows that imperfect alignment causes the orbital's footprint to disappear in the unnormalized spectra (Fig. 2, A and B). That is, the node is filled by the alignment distribution of ionizing molecules.

We now turn to the structures at higher electron momenta ($p_\perp > 0.5$ au) and ($|p_z| > 1.5$ au) in Fig. 2, C and D. This region is dominated by electrons that have rescattered. In Fig. 2, C and D, the relative probability of finding an electron in

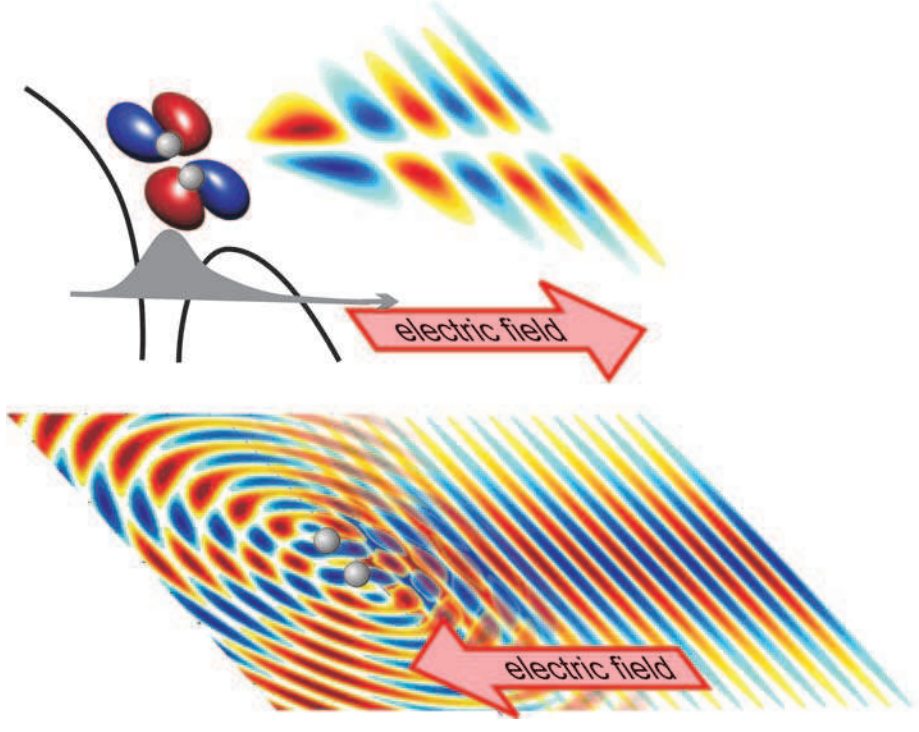

Fig. 1. (**Top**) Tunneling creates a filtered projection of the molecular orbital. Approximately half of the electron wave packet escapes directly to the detector. (**Bottom**) Remaining portion is driven back to the parent ion. Here, the central portion of the recolliding wave packet is shown diffracting from the molecule. The outer portions of the wave packet (not shown) weakly interact with the ion potential. The relative strength of each component depends on the filtered projection of the molecular orbital and therefore on molecular alignment.

the momentum region $p_z = 2$ au, $p_y = 1.5$ au in all quadrants and at $p_z = 0$ au, $p_x = 1$ au passes through rather broad local maxima. There are corresponding minima at $p_z = 2$ au, $p_x = 1.5$ au and at $p_z = 0$ au, $p_y = 1$ au. This structure contains information on the scattering potential. That is, we experimentally observed LIED.

Interpreting an electron distribution such as this is different from interpreting conventional electron diffraction because of the presence of the laser field (*17*). We analyzed our data in analogy to the attosecond streak camera (*21*) to remove the influence of the laser field on the electron momentum after the scattering has occurred. The final, observed momentum of a scattered electron is $\vec{p}_{fin} = \vec{p}_{rec} + \vec{A}_{rec}$ (*17*), where $\vec{A}_{rec} = (\vec{E}_0/\omega)\sin \omega t_{rec}$ is the vector potential defined by the electric field $\vec{E}(t) = \vec{E}_0 \cos(\omega t)$ of the probe pulse (here, ω is the frequency of the light), and $\vec{p}_{rec}$ is the electron momentum at the time t_{rec} of recollision. This analysis yields a manifold of momentum spheres centered at $p_z = \pm A_{rec}$ with radii p_{rec}. The maximum radius $p_{rec,max}$ corresponds to a recollision energy of $3.17U_p$ [where $U_p = (E_0/2\omega)^2$ is the ponderomotive potential]. Slicing the momentum spheres at perpendicular planes defined by $p_x \approx 0$ and $p_y \approx 0$ yields diffraction circles such as those illustrated in Fig. 4 (at left). Within each diffraction circle, we can relate our results to conventional electron diffraction: φ is the scattering angle, and the radius of each circle is the electron momentum or wavelength, $\lambda = h/p_{rec}$ (where h is Planck's constant), at which scattering occurs.

The four panels at right in Fig. 4 show the value of the measured electron distributions along diffraction circles of radius 1.4 au (blue), 1.2 au (red), and 1.0 au (black). Each curve is offset for clarity. Electrons in the range $0° < \varphi < 30°$ or $330° < \varphi < 360°$ are direct electrons and are not plotted in the figure (details in SOM text D).

Because the molecules were aligned along the y axis, the p_y-p_z projection is the most intuitive plane in which to analyze diffraction. At a recollision momentum p_{rec} of 1 au, the electron wavelength $\lambda = 6.3$ au is larger than twice the equilibrium bond length of O_2 ($d = 2.3$ au). However, numerical simulations (*22*, *23*) and experiments (*24*) have shown that the appropriate electron wavelength for diffraction is the wavelength at the core of the ion. That is, the recollision energy (corresponding to the radius of the diffraction circle) plus the ionization potential of the HOMO yield the appropriate diffraction wavelength. With this assumption ($\lambda = 4.57$ au), the first minimum at around 60° (and then at 300°) thus corresponds to a bond length of 2.6 au.

To help extend this interpretation, we turned to simulation (SOM text E). We used the probability of recollision as a function of the angle between the molecule and the laser electric field and averaged over the alignment distributions. The electron recollision momentum is chosen by selecting a diffraction circle for analysis. We made three final assumptions: (i) We assumed that the electron wavelength corresponds to the sum of recollision energy and the field free ionization energy. (ii) We assumed two-center diffraction. (iii) Because long trajectory electrons dominate, we concentrated on them. The resulting distributions are shown in the solid curves in Fig. 4. Comparing the calculated and measured distributions, we see that the modulation in the regions $\varphi \approx 50° - 150°$ and $\varphi \approx 210° - 310°$ arises from diffraction. The dashed lines highlight the shift of the diffraction maxima and minima with the electron wavelength. Electrons that backscatter through $\varphi \approx 180°$ are not properly described. They appear in the figure in the range $\varphi \approx 150° - 210°$. The overall agreement in the positions of the diffraction minima and maxima between simulations and experiment is good, except for N_2 in the p_x-p_z plane, where the simulated diffraction peaks appear shifted. This peak shift probably comes from an overestimation of the recollision probability for N_2 molecules oriented parallel to the laser field in the model.

There are three reasons why we obtain agreement for most angles. First, using normalized differences makes the two-center scattering contribution highly visible while making our results somewhat insensitive to details of the atomic contribution (*25*). Second, by concentrating on relatively high-energy electrons, we only need to consider the first recollision (*9*), keeping the electron trajectories relatively simple. Third, al-

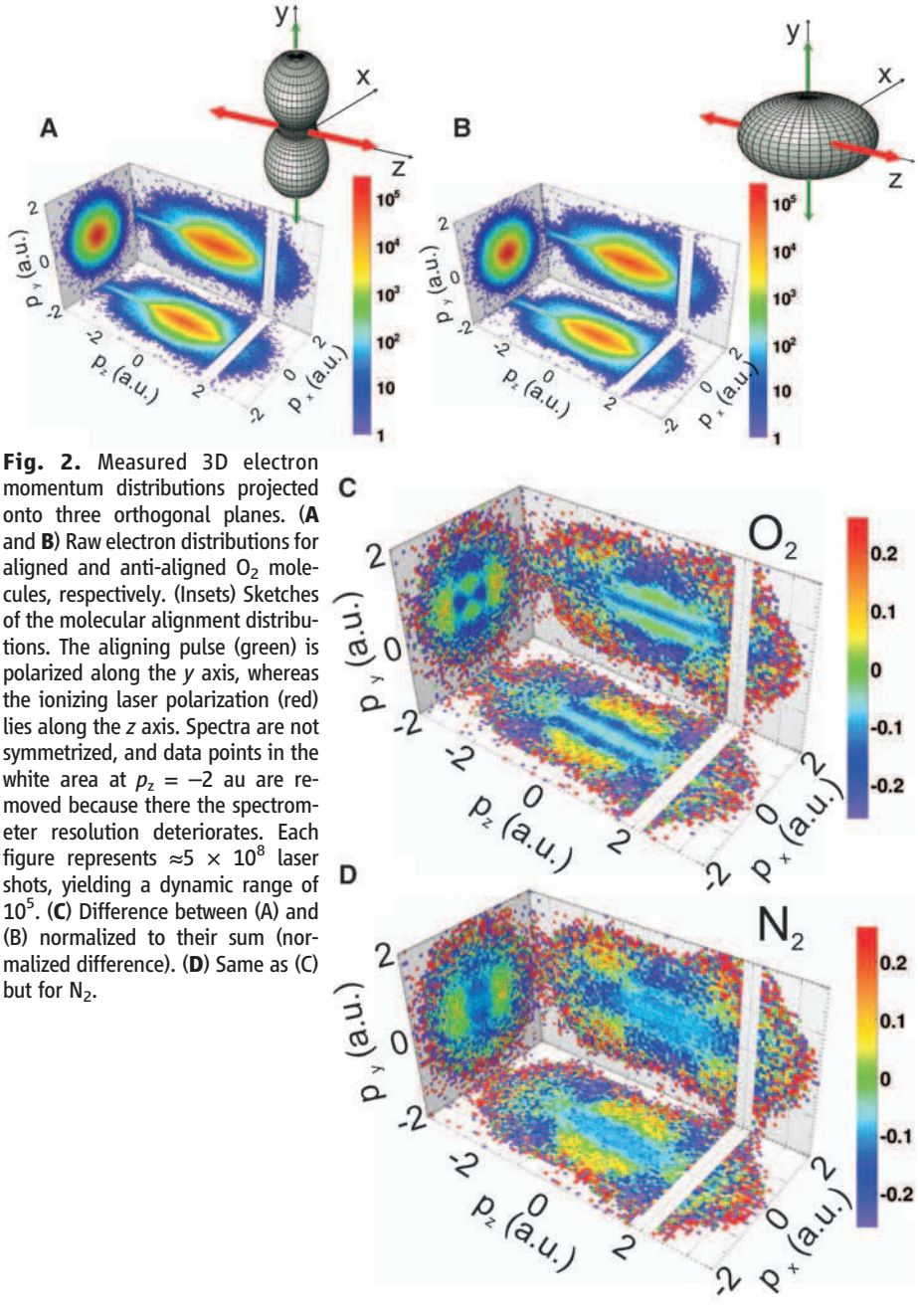

Fig. 2. Measured 3D electron momentum distributions projected onto three orthogonal planes. (**A** and **B**) Raw electron distributions for aligned and anti-aligned O_2 molecules, respectively. (Insets) Sketches of the molecular alignment distributions. The aligning pulse (green) is polarized along the *y* axis, whereas the ionizing laser polarization (red) lies along the *z* axis. Spectra are not symmetrized, and data points in the white area at $p_z = -2$ au are removed because there the spectrometer resolution deteriorates. Each figure represents $\approx 5 \times 10^8$ laser shots, yielding a dynamic range of 10^5. (**C**) Difference between (A) and (B) normalized to their sum (normalized difference). (**D**) Same as (C) but for N_2.

though the screened Coulomb potential is not fully treated in our diffraction analysis, we add the most important aspect by augmenting the electron energy measured from the scattering circles by I_p (*17*, *22*, *23*).

We have demonstrated that multiphoton ionization in the tunneling limit gives extensive information on the ionizing electronic orbital. If we rotate the molecule in small steps, all momenta from the wave function are sampled. We only need to select one angle for diffraction. This diffraction pattern reveals the interatomic dimensions of a molecule. Interestingly, the angle could be selected to favor recollision only from particular electronic configurations, allowing us to determine the structure of selected isomers or of excited states.

In a diffraction experiment, selecting a different electron wavelength λ changes the diffraction pattern in the same way as a change in the internuclear separation d ($\sin\varphi = n\lambda/d$, where n is the order of the diffraction peak). By showing that a 20% change in electron wavelength makes a measurable difference in the diffraction pattern, we indirectly demonstrate that vibrational or photochemical dynamics can be combined with LIED. Coincidence imaging allows us to use the characteristics of the correlated ion to select those events that we wish to analyze. Thus, LIED provides a method to isolate structural changes of any excited state that impresses a distinct signature on the ion.

In studies where coincidence imaging is unnecessary, employing a technology such as velocity map imaging (*26*, *27*) would allow electron spectra to be recorded using lasers with repetition rates as high as 136 MHz (*28*). Data of the same quality that we show could be obtained in milliseconds or less. Such a measurement is practical for any molecule that can be placed in the gas phase, provided that the strong field does not dislodge other electrons in an uncontrolled manner (*29*) and provided that the molecule can be aligned with sufficient precision.

Finally, we stand back and survey the emerging strong-field technology for molecular imaging. Tunneling, one of the most fundamental of the quantum mechanical processes, initiates all of the methods. Information about the ionizing orbital of the neutral molecule is imprinted on the tunneled electron. A second perspective on the molecular orbital is contained in the high-harmonic radiation that is produced upon recollision. High-harmonic radiation has two major advantages over tunneling. First, by measuring photons rather than electrons the problem of space-charge is avoided. Second, if the tunneled wave packet is independent of the angle between laser-field and molecular axis, tomography provides a well-developed algorithm for inverting the image (*11*, *30*). However, there is one major disadvantage: Tunneling and recombination are entwined in the angle-dependent harmonic spectrum (*31*). This problem has so far limited the application of orbital tomography.

A complementary insight is achieved by laser Coulomb explosion imaging (*32*–*34*) We become sensitive to the position of the nuclei in a molecular ion. LIED supplies us with the means to overcome the limitations of Coulomb explosion imaging and

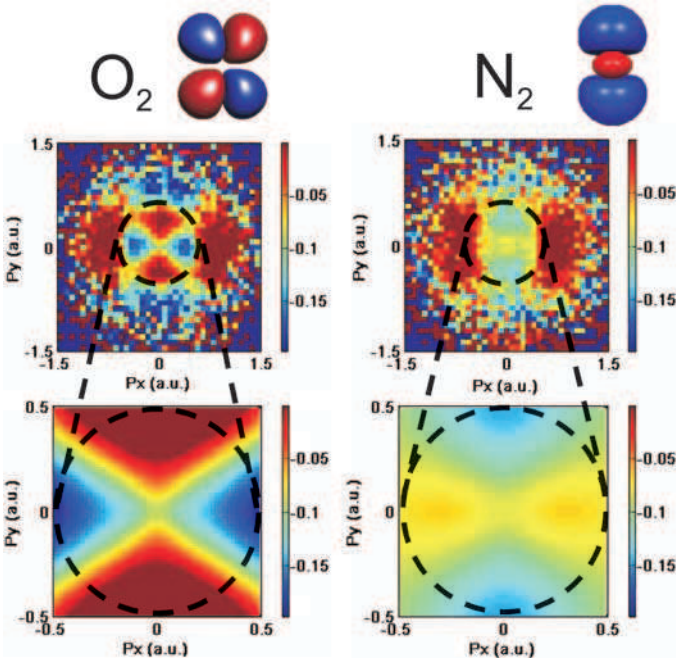

Fig. 3. p_x versus p_y projections of the normalized differences for O_2 and N_2. (**Top**) Experimental data (from Fig. 2). The color scale has been changed to emphasize the low lateral-momentum structure near the center of each figure enclosed in the dashed circle. The low lateral momentum retains the symmetry of the HOMO (shown above). (**Bottom**) Magnified results of our simulation (see text).

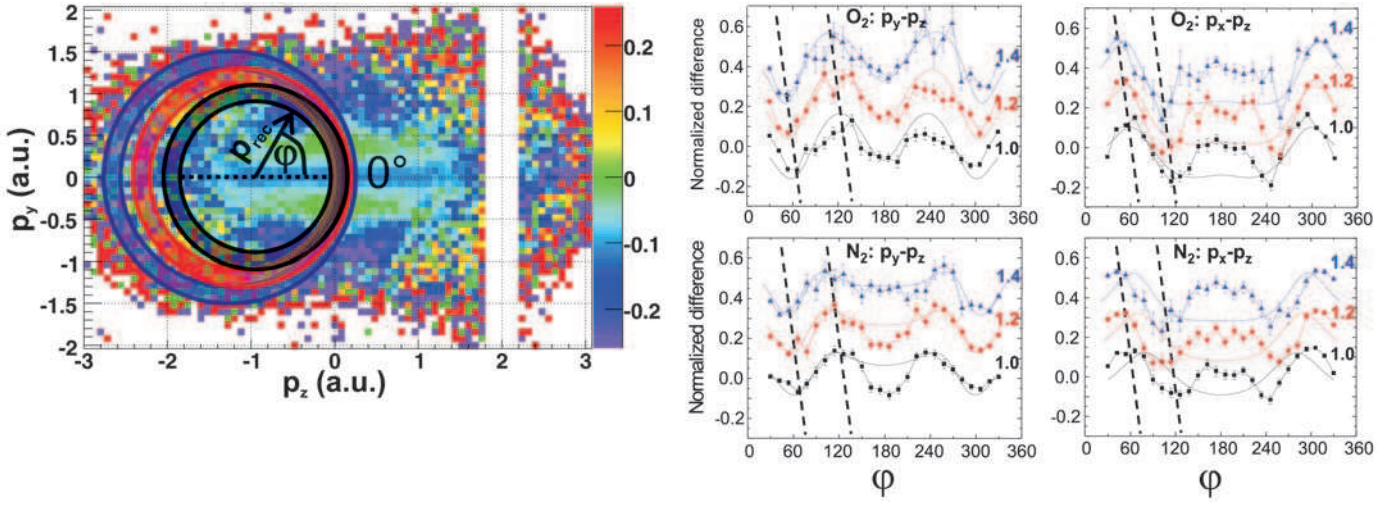

Fig. 4. Left panel is reproduced from Fig. 2C. Three color-coded diffraction circles are superimposed. The radius of the circle defines the recollision momentum p_{rec} (scattering wavelength); their width defines the range of momenta that are analyzed; and φ is the scattering angle. The four plots at right show the angular distributions within the indicated diffraction circles (see SOM text D for details). The color coding is preserved. Results of the simulations are superimposed as solid lines. The curves for recollision momentum of 1.0 au have no offset. For clarity, other curves are offset in units of 0.2. The data are shown with statistical error bars (1σ).

opens the pathway toward the imaging of larger molecules. Taken together, we can obtain a full picture of molecules. With the extension of these tools to pump-probe techniques, we will be able to simultaneously trace the temporal changes in the nuclear and electronic structure of molecules.

References and Notes

1. G. Binning, H. Rohrer, C. Gerber, E. Weibel, *Phys. Rev. Lett.* **49**, 57 (1982).
2. J. Muth-Böhm, A. Becker, F. Faisal, *Phys. Rev. Lett.* **85**, 2280 (2000).
3. X. Tong, Z. Zhao, C. Lin, *Phys. Rev. A* **66**, 033402 (2002).
4. A. Alnaser *et al.*, *Phys. Rev. A* **71**, 031403 (2005).
5. D. Pavičić, K. Lee, D. Rayner, P. B. Corkum, D. M. Villeneuve, *Phys. Rev. Lett.* **98**, 243001 (2007).
6. T. Zuo, A. Bandrauk, P. B. Corkum, *Chem. Phys. Lett.* **259**, 313 (1996).
7. H. Ihee *et al.*, *Science* **291**, 458 (2001).
8. B. J. Siwick, J. R. Dwyer, R. E. Jordan, R. J. D. Miller, *Science* **302**, 1382 (2003).
9. H. Niikura *et al.*, *Nature* **417**, 917 (2002).
10. P. B. Corkum, *Phys. Rev. Lett.* **71**, 1994 (1993).
11. J. Itatani *et al.*, *Nature* **432**, 867 (2004).
12. A. Staudte *et al.*, *Phys. Rev. Lett.* **99**, 263002 (2007).
13. A. Rudenko *et al.*, *Phys. Rev. Lett.* **99**, 263003 (2007).
14. J. Ullrich *et al.*, *Rep. Prog. Phys.* **66**, 1463 (2003).
15. H. Stapelfeldt, T. Seideman, *Rev. Mod. Phys.* **75**, 543 (2003).
16. N. B. Delone, V. P. Krainov, *J. Opt. Soc. Am. B* **8**, 1207 (1991).
17. M. Spanner, O. Smirnova, P. B. Corkum, M. Ivanov, *J. Phys. B* **37**, L243 (2004).
18. M. Ivanov, M. Spanner, O. Smirnova, *J. Mod. Opt.* **52**, 165 (2005).
19. T. Brabec, M. Ivanov, P. B. Corkum, *Phys. Rev. A* **54**, R2551 (1996).
20. D. Comtois *et al.*, *J. Phys. B* **38**, 1923 (2005).
21. J. Itatani *et al.*, *Phys. Rev. Lett.* **88**, 173903 (2002).
22. M. Lein, J. Marangos, P. Knight, *Phys. Rev. A* **66**, 051404 (2002).
23. S. Yurchenko, S. Patchkovskii, I. Litvinyuk, P. B. Corkum, G. Yudin, *Phys. Rev. Lett.* **93**, 223003 (2004).
24. D. Akoury *et al.*, *Science* **318**, 949 (2007).
25. M. Okunishi *et al.*, *Phys. Rev. Lett.* **100**, 143001 (2008).
26. C. Bordas, F. Paulig, H. Helm, D. Huestis, *Rev. Sci. Instrum.* **67**, 2257 (1996).
27. A. Eppink, D. Parker, *Rev. Sci. Instrum.* **68**, 3477 (1997).
28. I. Hartl *et al.*, *Opt. Lett.* **32**, 2870 (2007).
29. M. Lezius *et al.*, *Phys. Rev. Lett.* **86**, 51 (2001).
30. T. Kanai, S. Minemoto, H. Sakai, *Nature* **435**, 470 (2005).
31. S. Baker *et al.*, *Science* **312**, 424 (2006), published online 1 March 2006; 10.1126/science.1123904.
32. F. Légaré *et al.*, *Phys. Rev. A* **72**, 052717 (2005).
33. T. Ergler *et al.*, *Phys. Rev. Lett.* **97**, 193001 (2006).
34. A. Alnaser *et al.*, *Phys. Rev. A* **72**, 030702 (2005).

35. We gratefully acknowledge financial support from the Canadian Institute for Photonics Innovation, Natural Sciences and Engineering Research Council of Canada, Canadian Foundation for Innovation, Alexander-von-Humboldt Foundation, Deutsche Forschungsgemeinschaft, and the German Academic Exchange Service. P.B.C. acknowledges financial support from the Air Force Office of Scientific Research. M.M. thanks the German National Academic Foundation.

Supporting Online Material

www.sciencemag.org/cgi/content/full/320/5882/1478/DC1
SOM Text
Figs. S1 to S3
References

18 March 2008; accepted 16 May 2008
10.1126/science.1157980

Electrical Resistance of Long Conjugated Molecular Wires

Seong Ho Choi, BongSoo Kim, C. Daniel Frisbie*

The charge transport mechanism of a wire can be revealed by how its electrical resistance varies with length. We have measured the resistance and current-voltage characteristics of conjugated molecular wires ranging in length from 1 to 7 nanometers, connected between metal electrodes. We observe the theoretically predicted change in direct-current transport from tunneling to hopping as a function of systematically controlled wire length. We also demonstrate that site-specific disruption of conjugation in the wires greatly increases resistance in the hopping regime but has only a small effect in the tunneling regime. These nanoscale transport measurements elucidate the role of molecular length and bond architecture on molecular conductivity and open opportunities for greater understanding of electrical transport in conjugated polymer films.

Charge transport can occur through long, π-conjugated molecules (*1*–*3*), and the term "molecular wire" is often used to describe conjugated molecules in which charge transport is efficient over long distances (*4*, *5*). For example, the β-carotene molecule can transfer electrons over tens of Angstroms (*6*). In the context of molecular electronics, where the ultimate goal is the fabrication of circuitry based on the prescribed electronic function of individual molecules (*4*, *7*), it is desirable to have a quantitative definition of what constitutes a molecular wire.

A fundamental property of a wire is the scaling of its resistance (or conductance) with length. The length dependence of resistance is a direct consequence of the charge transport mechanism. In the macroscopic world, the resistance of a metallic wire increases linearly with length as a result of the diffusive nature of carrier transport in the metal. However, this particular scaling need not hold for conduction in molecules over nanometer-length scales, as has been pointed out theoretically (*8*–*10*) and observed experimentally (*2*, *3*, *11*, *12*). For short molecules (<3 nm) connected between metallic contacts, it is well-accepted that resistance scales exponentially with length according to Eq. 1.

$$R = R_0 \exp(\beta L) \quad (1)$$

where R is the junction resistance, R_0 is an effective contact resistance, L is molecular length, and β is the exponential prefactor that depends on the nature of bonding in the molecular backbone. The exponential length dependence in Eq. 1 results directly from the transport mechanism in metal/molecule/metal junctions based on short molecules, namely, direct (nonresonant) tunneling.

For longer molecules connected between metal electrodes, the scaling of resistance with length can be anticipated by comparison to fundamental studies of electron transfer in solution. Both theory and experiment on soluble donor-bridge-acceptor (D-B-A) systems (*2*, *3*, *8*, *11*, *12*) indicate that for long molecular bridges, the charge transport mechanism changes from direct tunneling to hopping, as evidenced by a change in the length dependence of the electron transfer rate constant. Specifically, for short bridges, the length dependence is exponential, corresponding to the tunneling regime, and for long bridges, the scaling is linear, as expected for hopping transport; in the experiments reported by Wasielewski and colleagues (*2*), the transition occurs when the conjugated bridge becomes longer than ~2.5 nm. The weaker length dependence associated with the hopping regime facilitates the transport of charge over greater distances, and it is this regime that might be considered most "wirelike," although tunneling through saturated peptide bonds, for example, has also been shown to provide enhanced transport over relatively large distances in redox proteins (*13*, *14*).

In the context of molecular electronics, it has been difficult to systematically examine the hopping regime in conjugated molecular wires connected to metallic contacts because of the relatively large range of molecular lengths required (spanning many nanometers) and the complexities of adsorbing long molecules to metal surfaces while controlling orientation. Electrical transport measurements on molecules up to 18 nm in length have been reported (*15*), and charge hopping in molecular junctions has been observed (*16*–*18*), but the systematic length dependence of conduction has not been a principal focus.

Here, we provide direct evidence for a change in transport mechanism from tunneling to hopping in molecular junctions based on conjugated oligophenyleneimine (OPI) wires ranging in length from 1.5 to 7.3 nm. We contacted OPI

Department of Chemistry and Department of Chemical Engineering and Materials Science, University of Minnesota, Minneapolis, MN 55455, USA.

*To whom correspondence should be addressed: frisbie@cems.umn.edu

Laser Induced Electron Tunneling and Diffraction
- Supporting Online Material -

Supporting Text A: Materials and Methods

We determined the momentum vectors of electrons and ions in coincidence using COLTRIMS (*S1*). Electrons and ions created in the laser focus were guided to separate time and position sensitive microchannel plate detectors with delayline readout by weak electric (29.1 V/cm) and magnetic (13.7 Gauss) fields. After an acceleration region of 68.5 mm, electrons entered an electric field free drift tube with a length of 151.5 mm before reaching the detector (RoentDek HEX80 (*S2*)). Ions were accelerated over a path of 148 mm onto a RoentDek DLD80 detector, without passing through a field-free drift region. Both detectors had an active diameter of 80 mm.

We determined the following electron momentum resolutions: $\Delta \mathrm{p}_x = \Delta \mathrm{p}_y = 0.2$ au; $\Delta \mathrm{p}_z = 0.36$ au. The latter is measured as the FWHM of the center of mass momentum distribution of O_2^+ ions in the time of flight direction. The resolution in the x-y directions is calculated from the respective detector resolutions since the center of mass momentum distributions are dominated by the resolution of the ion momentum[1]. To discriminate against false coincidences, we only use events for electron spectra whose electron-ion center of mass momentum in the time of flight direction (p_z) is no more than ± 0.4 au.

Our jet contained, among other species, N_2 and O_2 at the same time. Therefore, oxygen and nitrogen were measured under exactly the same conditions. The ion time of flight allows identification of the ion species and thereby determination of the origin of the measured electron. The electrons in the spectra of Fig.2 are correlated to either $^{16}O_2^+$ or $^{14}N_2^+$.

Supporting Text B: Molecular Alignment

We used the following pump-probe delays to align or anti-align molecules: O_2 aligned 2.929 ps, anti-aligned 8.726 ps; N_2, aligned 3.856 ps, anti-aligned 4.490 ps. Each delay was maintained for ten seconds whereafter a computer-controlled delaystage moved to the next. Thereby a

[1]The center of mass momentum distributions (electron momentum + ion momentum) yield FWHM $\Delta \mathrm{p}_x = 2.6$ au, $\Delta \mathrm{p}_y = 4.4$ au (jet direction) and $\mathrm{p}_z = 0.36$ au (time of flight direction).

possible drift of the experimental parameters, as e.g. the laser pulse energy, affects the data equally for all four measurements. As each alignment was given the same amount of measuring time, our spectra are by default normalized to the same number of laser shots. Note, that the absolute ionization yields should not be compared between N_2 and O_2, since the densities of the two species in the jet were not equal.

During the experiment a fraction of the molecules was doubly ionized by the probe pulse and Coulomb exploded thereafter. The recorded N^+ and O^+ ion fragments were used to obtain the alignment distributions. Assuming the axial recoil approximation the momentum vectors point along the former molecular axis. In Fig. S2 only correlated fragments are shown, i.e. events where two N^+ or two O^+ were produced by a single laser shot with a center of mass (CM) momentum $p_{CM} \leq 10$ au and a kinetic energy release of 5.1 eV<KER<13.1 eV. The alignment angle θ is the angle between the alignment direction (y-axis) and the ion momentum, i.e. the molecular axis, projected into the x-y plane. At $\theta = 0°$, the molecule points along the alignment direction. Fig. S2(a) shows the alignment distribution of oxygen, while Fig. S2(b) presents the observed alignment distributions for nitrogen. For a detailed discussion of nonadiabatic alignment the reader is referred to refs. (*S3, S4*).

Supporting Text C: Simulation of the Direct Electron's Lateral Momentum Distributions

We used a velocity-Verlet algorithm to compute the classical electron trajectories making up the quantum wave packet after tunneling ionization, under the influence of both the laser field and the parent ion's Coulomb potential. The electron trajectories are calculated starting at the classical exit point of the tunnel for all phases of birth and weighted according to the tunneling ionization rate in each case (*S5*). For each phase of birth a subset of trajectories is launched with a lateral momentum distribution corresponding to the tunnel-filtered projection of the ionized molecule's momentum-space orbital (equation 1 in the main text). The orbital is calculated using GAMESS and Fourier-transformed before being projected and filtered, for all angles between the laser field and molecular axis. The wave packet's final lateral momentum distribution is calculated for each case and averaged, taking into account the three-dimensional molecular orientation distributions for alignment or anti-alignment, as well as the ionization rate dependence on molecular orientation for each molecule. Finally, the normalized difference between the results obtained for molecular alignment and anti-alignment is computed to yield the plots shown in Fig. 3.

While the simulation is complete with regard to including the alignment distributions and the influence of the parent ion's Coulomb field on the final electron momentum, the key structures observed in the low energy electron can be understood by a very simple model. In Fig. S3 we have illustrated this. To calculate the momentum distribution of an electron tunneled from the HOMO, we first calculate the momentum representation of the HOMO via Fourier transformation. Second, we apply the gaussian filter of the suppressed barrier in equation 1 in projection

to the HOMO according to the alignment in question (left panels in Fig. S3). When considering parallel alignment of molecular axis and laser field the resulting momentum distribution has to be cylindrically symmetrized (center panels in Fig. S3). Finally, subtracting the momentum distributions shows the major features of the experiment even for such a simplified analysis (right panels in Fig. S3).

In the experiment, the measurement is done over ensembles of aligned and anti-aligned molecules. Therefore, the structures in the experimental difference spectra tend to be blurred compared to Fig. S3. In addition to this, the simulations show that the image of an orbital projected into the electron wave packet by tunneling is slightly distorted by the weak Coulomb attraction between large impact parameter recolliding electrons and their parent ion (also called Coulomb focusing (*S6, S7*)). Experimentally, the influence of Coulomb focusing can be minimized in p_x-p_y projections taken for large longitudinal momenta ($\mathrm{p}_z > 1$ au). Using elliptically polarized or longer wavelength light the influence of Coulomb focusing on the nascent structure of the wave function can be further minimized.

Supporting Text D: Analysis of Diffraction

In momentum space, diffraction patterns are mapped onto a sphere with a radius corresponding to the electron momentum upon recollision p_{rec}. The origin of this sphere is shifted, or streaked by the laser field by $\mathrm{p}_{z0} = E_0/\omega \sin\phi_{rec}$, where ϕ_{rec} is the laser phase at the instant of recollision, E is the peak electric field in the laser pulse and ω the laser frequency (*S8*). We calculate the shifts p_{z0} for given recollision momenta of 1.0, 1.2 and 1.4 au assuming long trajectories and a probe pulse intensity of $I = 2.5 \times 10^{14}$ W/cm^2.

To obtain the diffraction circle in the x-z plane from our experimental data, we transform to spherical coordinates centered around p_{z0}:

$$\rho = \sqrt{\mathrm{p}_x^2 + \mathrm{p}_y^2 + (\mathrm{p}_z - \mathrm{p}_{z0})^2} \tag{S1}$$

$$\vartheta = \arccos\left(\frac{\mathrm{p}_y}{\rho}\right) \tag{S2}$$

$$\varphi = \arctan\left(\frac{\mathrm{p}_x}{\mathrm{p}_z - \mathrm{p}_{z0}}\right) \tag{S3}$$

We select only electrons obeying $\rho = \mathrm{p}_{z0} \pm 0.1$ au and $\vartheta = 90° \pm 45°$. That is, only electron momenta within a spherical shell of radius $\mathrm{p}_{rec} \pm 0.1$ au, centered around p_{z0} and cut by two cones contribute to the diffraction circles. The scattering angle φ as plotted in Fig. 4 is the azimuth corresponding to this coordinate system.

Due to inversion symmetry along the p_z axis (i.e. the polarization direction of the ionizing pulses), this procedure can be repeated with inverted p_z coordinates. We add the diffraction circles centered around p_{z0} and $-\mathrm{p}_{z0}$ for improved statistics. After this, the spectra for aligned and anti-aligned molecular distributions are set to the same integral value. Finally, we calculate

normalized differences between the aligned and the anti-aligned case. Data points at a scattering angle of $\varphi < 30^\circ$ are not plotted as they are dominated by direct, non-rescattered electrons. The errorbars shown in Fig. 4 are purely statistical and were calculated using Gaussian error propagation and assuming Poisson statistics (the standard deviation σ of a bin containing n electrons is $\sqrt{n}$). The same procedure is repeated accordingly for the y-z plane.

Supporting Text E: Simulation of the Rescattered Electron Waves

An electron plane wave of intensity I_o scattered by a rigid molecule can be expressed as a function of the scattering electron momentum transfer $\vec{\mathrm{s}} = \vec{\mathrm{p}}_i - \vec{\mathrm{p}}_f$, where $\vec{\mathrm{p}}_i$ and $\vec{\mathrm{p}}_f$ are the incident and scattered electron momentum vectors, respectively (*S9*). It depends as follows on the $\vec{\mathrm{r}}_{ij}$ vectors linking each pair of i-th and j-th atoms in the molecule and the atomic scattering factors $f_i(|\vec{\mathrm{s}}|)$:

$$I(\vec{\mathrm{s}}) \propto I_0 \sum_{i=1}^{N} \sum_{j=1}^{N} f_i(|\vec{\mathrm{s}}|) f_j^*(|\vec{\mathrm{s}}|) \exp\left(i\vec{\mathrm{s}} \cdot \vec{\mathrm{r}}_{ij}\right) \tag{S4}$$

In the case of a homonuclear diatomic (N=2) with vector $\vec{\mathrm{d}}$ between the two atoms, the formula can be written as:

$$I(\vec{\mathrm{s}}) \propto I_0 |f(|\vec{\mathrm{s}}|)|^2 \left[1 + \cos(\vec{\mathrm{s}} \cdot \vec{\mathrm{d}})\right] \tag{S5}$$

In order to simulate the LIED curves obtained from the experimental data extracted along the diffraction circles, we use this formula, neglecting the first two factors. They do not depend on molecular orientation and cancel out in the normalized differences. The last factor in eq. S5 is therefore computed as a function of the electron scattering angle and averaged over all orientations in the aligned and anti-aligned distributions, taking into account the angular-dependent recollision probability. For a diffraction circle with radius p_{rec}, the simulation assumes an effective Coulomb-accelerated recollision energy given by $E_{kin} = \mathrm{p}_{rec}^2/2 + I_p$.

References

S1. J. Ullrich, *et al.*, *Rep. Prog. Phys.* **66**, 1463 (2003).

S2. Roentdek GmbH, 65779 Kelkheim, Germany, www.roentdek.com.

S3. P. W. Dooley, *et al.*, *Phys. Rev. A* **68**, 023406 (2003).

S4. H. Stapelfeldt, T. Seideman, *Rev. Mod. Phys.* **75**, 543 (2003).

S5. M. Ammosov, N. Delone, V. Krainov, *Sov. Phys. JETP* **64**, 1191 (1986).

S6. T. Brabec, M. Ivanov, P. Corkum, *Phys. Rev. Lett.* **54**, R2551 (1996).

S7. D. Comtois, *et al.*, *J. Phys. B* **38**, 1923 (2005).

S8. M. Spanner, O. Smirnova, P. Corkum, M. Ivanov, *J. Phys. B* **37**, L243 (2004).

S9. I. Hargittai, M. Hargittai, *Stereochemical Applications of Gas-Phase Electron Diffraction* (Wiley-VCH, 1988).

Supporting Figures

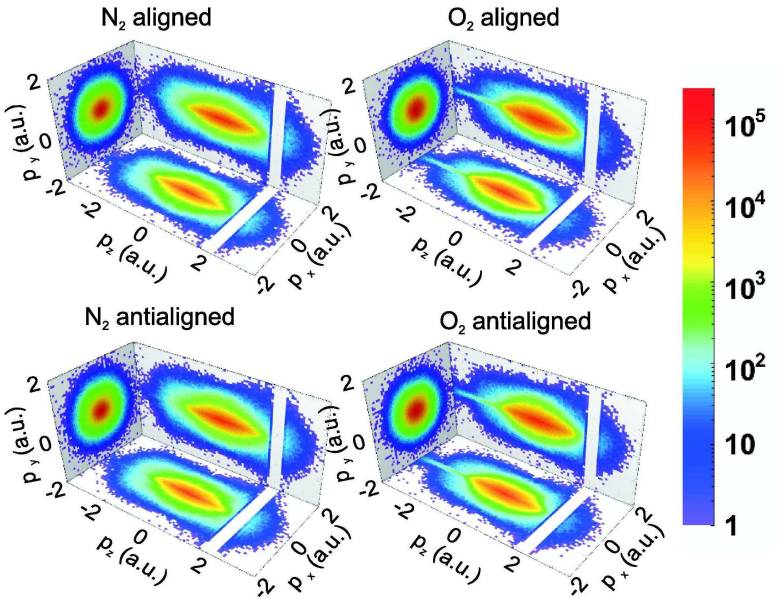

Figure S1: Raw electron momentum distributions for both molecules and the two alignments. All data sets are shown on the same color scale. The exponential fall-off in the signal for momenta larger than zero is due to the strong dependence of the ionization probability on the instantaneous field strength.

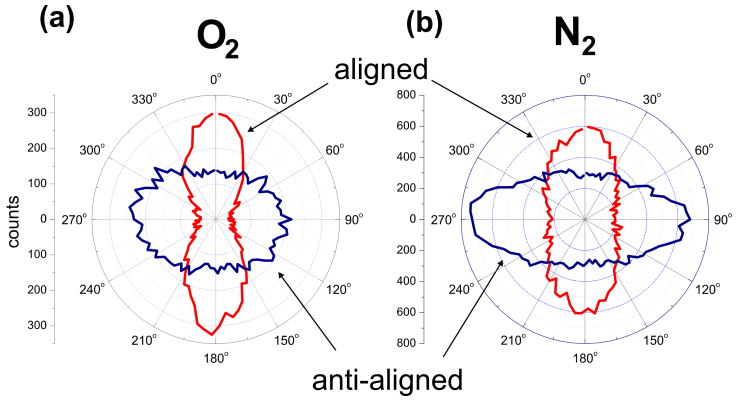

Figure S2: Measured angular distributions of the molecular alignment for (a) aligned (red) and anti-aligned (blue) O_2 and (b) aligned (red) and anti-aligned (blue) N_2 molecules. The aligning pulse polarization is along the vertical axis.

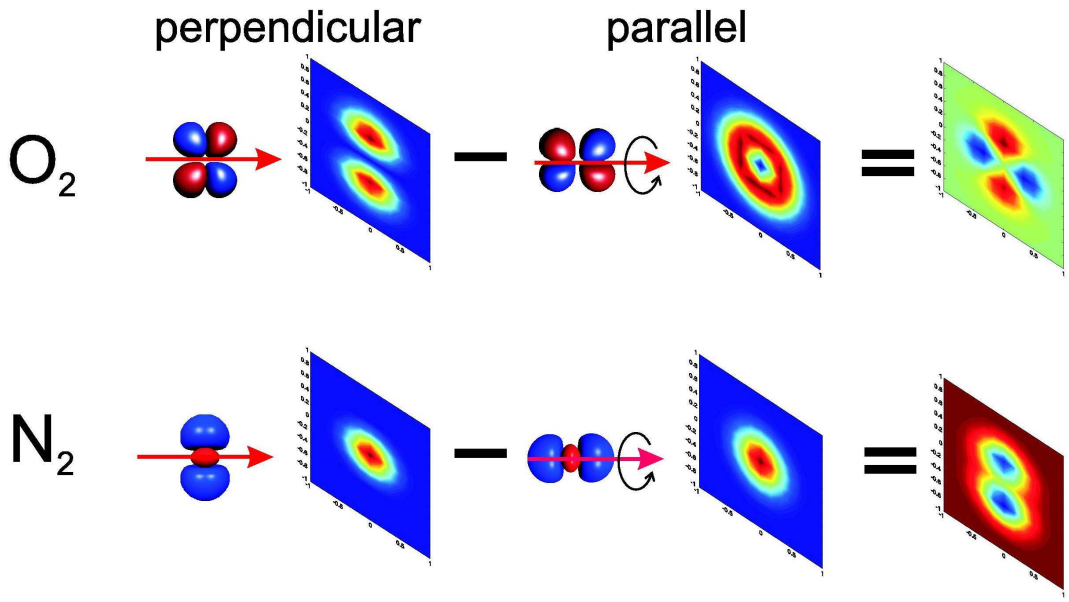

Figure S3: Shown are the momentum distributions directly after tunneling for two different alignments and the two molecules. A molecule perpendicular to the field represents the aligned distribution and a molecule parallel to the field represents anti-alignment. The phase between the different parts of the tunneled wave packet cannot be observed and therefore does not show up in the momentum distributions. The patterns obtained from the difference between the two single molecular orientations are similar to the experimental measurement, which contains the contributions from all molecules in the alignment / anti-alignment distributions. They directly reflect the symmetry of the HOMO that has been ionized.